ACS APPLIED NANO MATERIALS

www.acsanm.org Article

MoS_2 Nanoflake and ZnO Quantum Dot Blended Active Layers on AuPd Nanoparticles for UV Photodetectors

Shusen Lin, Rutuja Mandavkar, Rakesh Kulkarni, Shalmali Burse, Md Ahasan Habib, So Hee Kim, Ming-Yu Li, Sundar Kunwar,* and Jihoon Lee*

Cite This: https://doi.org/10.1021/acsanm.1c03748 Read Online

ACCESS | Metrics & More | Article Recommendations | Supporting Information

ABSTRACT: A hybrid UV photodetector incorporating a blended active layer of molybdenum disulfate (MoS_2) nanoflakes and zinc oxide (ZnO) quantum dots (QDs) on the Au core−shelled AuPd hybrid NPs (HNPs), namely, the MoS_2*ZnO/HNP configuration, is demonstrated for the first time. In the proposed configuration, the hot carriers generated by the strong localized surface plasmon resonance (LSPR) of Au-shelled AuPd HNPs can be effectively collected at the ZnO QD's conduction band. The blended MoS_2 nanoflakes also successfully absorb the high-energy photons, offering additional photocarriers. The optimized device demonstrates an increased photocurrent (I_{ph}) of 1.49×10^{-3} A at 10 V under 54.9 mW/mm^2, which offers improved performance parameters of a photoresponsivity (R) of 2,525 mA/W, a detectivity (D) of 7.251×10^{11} jones, and an external quantum efficiency (EQE) of 813% at 0.34 mW/mm^2. The result is one of the best ZnO-based photodetectors demonstrated so far. The enhanced photocurrent is due to the greater photocarrier injections by the blended active layer of MoS_2 nanoflakes and ZnO QDs on the Au-shelled AuPd HNPs. The finite-difference time-domain (FDTD) simulation confirms the significantly increased maximum local e-field intensity and hotspots of the MoS_2*ZnO/HNP blended active layer.

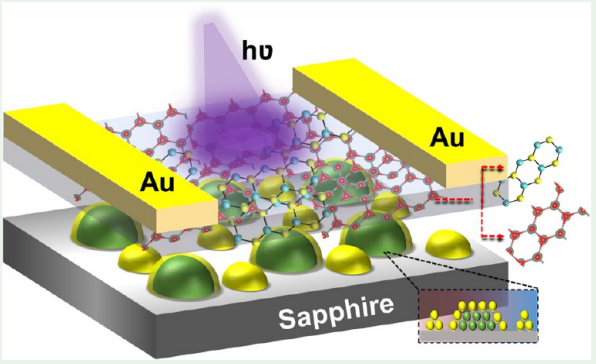

KEYWORDS: *blended active layer, molybdenum disulfate nanoflakes, zinc oxide quantum dots, AuPd hybrid NPs, UV photodetectors*

UV photodetectors offer a broad range of applications in various fields from flame detection, water sterilization, pollution monitoring, and biomolecule sensing to factory automatization, intersatellite communication, and missile launch detection.[1−5] The UV photodetectors with high photocurrent, rapid response, and low cost are the essential components to meet the demands of practical applications. Over the years, a number of material systems have been investigated for the UV photodetector configurations such as transition-metal dichalcogenides (TMD), halides, perovskites, metal oxides, and silicon derivatives.[1−7] Recently, various metal oxide semiconductors including CuO, TiO_2, $BaTiO_3$, and ZnO have received much-increased research attention due to their superior UV photon absorption characteristics of photoresponsivity, detectivity, and quantum efficiency.[1−7] More recently, the hybrid UV photodetector configurations consisting of various compatible nanomaterial systems have been drawing significant research interest due to their added functionality, tunability, and device performance, i.e., electronic heterogeneity, site-specific response, and combinational effect of constituent materials. ZnO, a group II-VI semiconductor with a wide band gap of 3.37 eV, has been widely adapted for UV photodetector applications.[6,8−10] A variety of approaches have been attempted to improve the performance of ZnO-based photodetectors including surface functionalization, nanocrystallization, heterojunction, counter doping, hybrid configurations, etc.[6,8−10] For example, the hybrid structure of BTO-coated ZnO quantum dots (QDs) exhibited a significantly improved response speed, which was attributed to the reduced carrier recombination time.[8] The hybrid configuration of ZnO QDs and graphene QDs on the keratin nanofiber textile resulted in a transparent and flexible ultraviolet photodetector.[9] At the same time, the plasmonic metallic nanoparticles (NPs) can demonstrate a strong localized surface plasmon resonance (LSPR) and thus can induce considerably increased photocarrier injection.[11−14] The rapid charge transfer of hot electrons by the strong LSPR can offer substantially improved photocurrent. Among various plasmonic NPs, Au NPs can demonstrate the strong LSPR[11−14] and exhibit strong absorption in the UV and vis region due to the quadrupolar and dipolar plasmonic resonance modes.

Received: November 6, 2021
Accepted: January 6, 2022

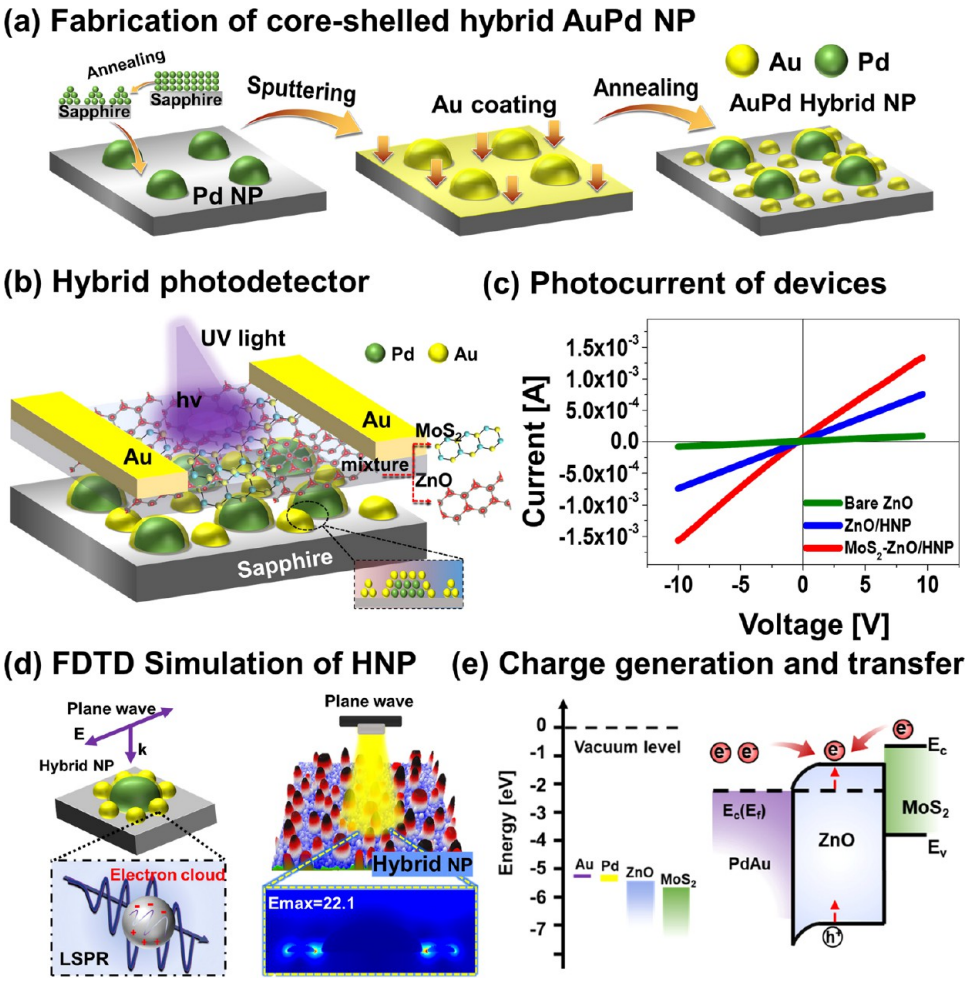

Figure 1. (a) Fabrication of core−shelled AuPd hybrid nanoparticles (HNPs) with the background Au nanoparticles. (b) Schematic of hybrid UV photodetector (PD) incorporating the mixture layer of molybdenum disulfate (MoS_2) nanoflakes (NFs) and zinc oxide (ZnO) quantum dots (QDs) on the core−shelled AuPd HNPs. (c) Photocurrent of bare ZnO, ZnO/HNPs, and MoS2*ZnO/HNPs photodetector under UV irradiation. (d) Finite-difference time-domain (FDTD) simulation of HNPs. (e) Work function of deposited materials and the carrier generation and transfer process.

Meanwhile, the molybdenum disulfate (MoS_2) nanostructures as a two-dimensional (2-D) transition-metal dichalcogenide (TMD) semiconductor also may demonstrate their value in UV photodetection applications with increased photogenerated carriers.[15,16] In this respect, a hybrid configuration incorporating the blended active layer of MoS_2 nanoflakes (NFs) and ZnO QDs on the Au core−shelled AuPd hybrid NPs (HNPs), namely, MoS_2*ZnO/HNP configuration, in a single device would be a promising attempt to utilize the significantly increased photocarriers offered by these materials. A hybrid NP configuration incorporating the highly dense Au NPs along with the MoS_2 nanoflakes and ZnO QDs in a single device configuration can be largely beneficial to utilize the strong LSPR and photocarrier injection for the improved UV photodetector performance.

In this work, the MoS_2 nanoflake (NF) and ZnO quantum dot (QD) blended active layer on the core−shelled AuPd hybrid NPs (HNPs) is demonstrated for the first time for UV photodetectors. The optimized MoS_2*ZnO/HNP device demonstrates a greatly enhanced photocurrent (I_{ph}) of 1.49 $\times 10^{-3}$ A. As a result, an outstanding photoresponsivity (R) of 2,525 mA/W, a detectivity (D) of 7.251 $\times 10^{11}$ jones, and an external quantum efficiency (EQE) of 813% at 0.34 mW/mm^2 are exhibited. The core−shelled AuPd HNPs template is prepared via a dual-phase solid-state dewetting (SSD) approach and offers the Au NPs with exceptionally high density along with the Au-shelled AuPd NPs, as illustrated in Figure 1a. Then, the blended active layer of MoS_2 NFs and ZnO QDs is deposited on the AuPd HNPs to provide the conductive channel and to collect the injected photocarriers, as shown in Figure 1b. Along with the addition of each component, a sharp increase in the photocurrent (I_{ph}) is clearly observed, as seen in Figure 1c. The FDTD simulation shows a significantly enhanced local e-field intensity and hotspot distribution by the MoS_2*ZnO/HNP blended active layer, as shown in Figure 1d. The mixed layer of MoS_2 nanoflakes and ZnO QDs on the Au-shelled AuPd hybrid NPs can significantly improve the photodetector characteristics by utilizing the increased hot carriers by the LSPR and photocarrier injection, as described in Figure 1e.

RESULTS AND DISCUSSION

Starting from the identical Pd NP templates, two distinctive configurations of AuPd NP are demonstrated depending on the Au coating thickness and a postannealing process. Fully alloyed AuPd NPs are presented in Figure 2, and Au-shelled

https://doi.org/10.1021/acsanm.1c03748
ACS Appl. Nano Mater. XXXX, XXX, XXX−XXX

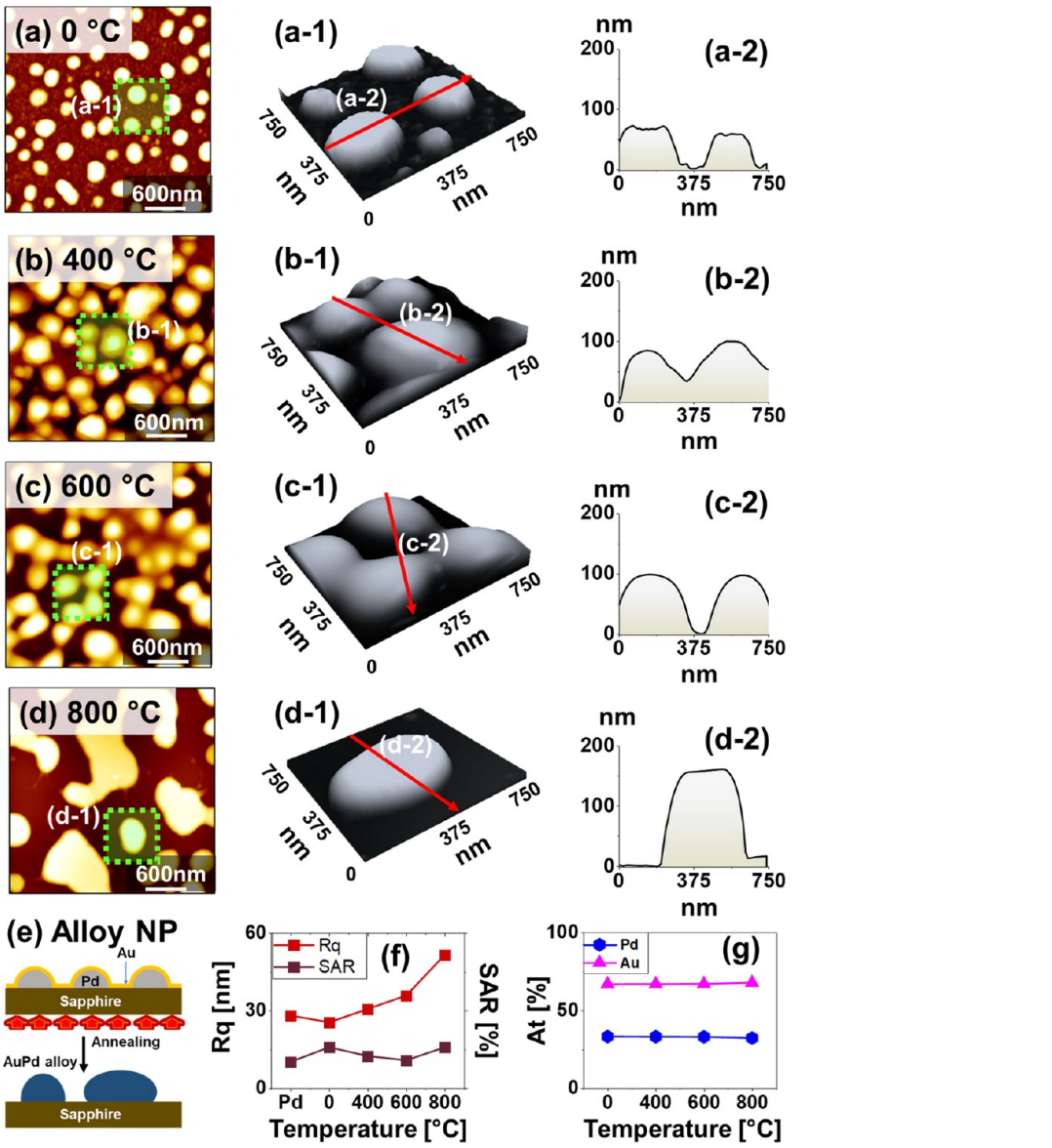

Figure 2. Surface morphology evolution of fully alloyed AuPd NPs by 30 nm Au coating on a 30 nm Pd NP template and subsequent annealing between 0 and 800 °C. (a–d) Atomic force microscopy (AFM) top views of 3 × 3 μm^2. ((a-1)–(d-1)) Enlarged side views of 750 × 750 nm^2. ((a-2)–(d-2)) Cross-sectional line profiles from the side views. (e) Schematic illustration of fully alloyed AuPd NP formation. (f) Summary plots of RMS roughness (R_q) and surface area ratio (SAR). (g) Summary plots of the atomic percentages of Au and Pd.

AuPd hybrid NPs are shown in Figure 3, which were fabricated during the second phase of solid-state dewetting (SSD) by controlling the Au coating thickness and postannealing process. The fully alloyed AuPd NPs indicate that the NP elements are fully alloyed in terms of atomic distribution. In the core–shelled AuPd hybrid NP configuration, the Pd NPs are shelled by the Au layer through the unique dual-phase SSD approach, which can offer very high-density background Au NPs. Consequently, a significantly increased hop spot distribution and much-increased maximum local e-field intensity are demonstrated. Normally, this high-density Au NP with a very small size is not available based on the general SSD.

Initially, the Pd NPs were fabricated on sapphire (0001) by annealing a 30 nm Pd film at 800 °C based on the SSD.[17] As the deposited Pd films are metastable, the existing voids and pinholes in the thin Pd films serve as nucleation centers in the process of SSD well below the melting point of Pd (1555 °C), induced by the atomic diffusion of adatoms upon annealing. As mass transport of adatoms occurs, the voids can grow larger and merge with the adjacent voids, leading to the construction of isolated nanoislands. Along with the reduction of surface and interface energies, the energetically stable semispherical configuration of Pd NPs can be formed based on the SSD.[17] The Pd NPs had an average height and diameter of ∼90 and 350 nm, respectively, as shown in Figure S2, and two LSPR peaks in the UV at ∼330 nm and VIS at ∼450 nm were observed, which is in agreement with the quadrupolar resonance (QR) and dipolar resonance (DR) plasmonic modes.[18,19]

The Pd NPs were utilized as a template for further growth, i.e., the deposition of Au films of various thicknesses and subsequent annealing for the second phase of SSD. Here, a slight change in the Au coating thickness was found to be the crucial factor for the determination of the resulting NP configuration. For instance, the Au coating thickness above 10

https://doi.org/10.1021/acsanm.1c03748
ACS Appl. Nano Mater. XXXX, XXX, XXX–XXX

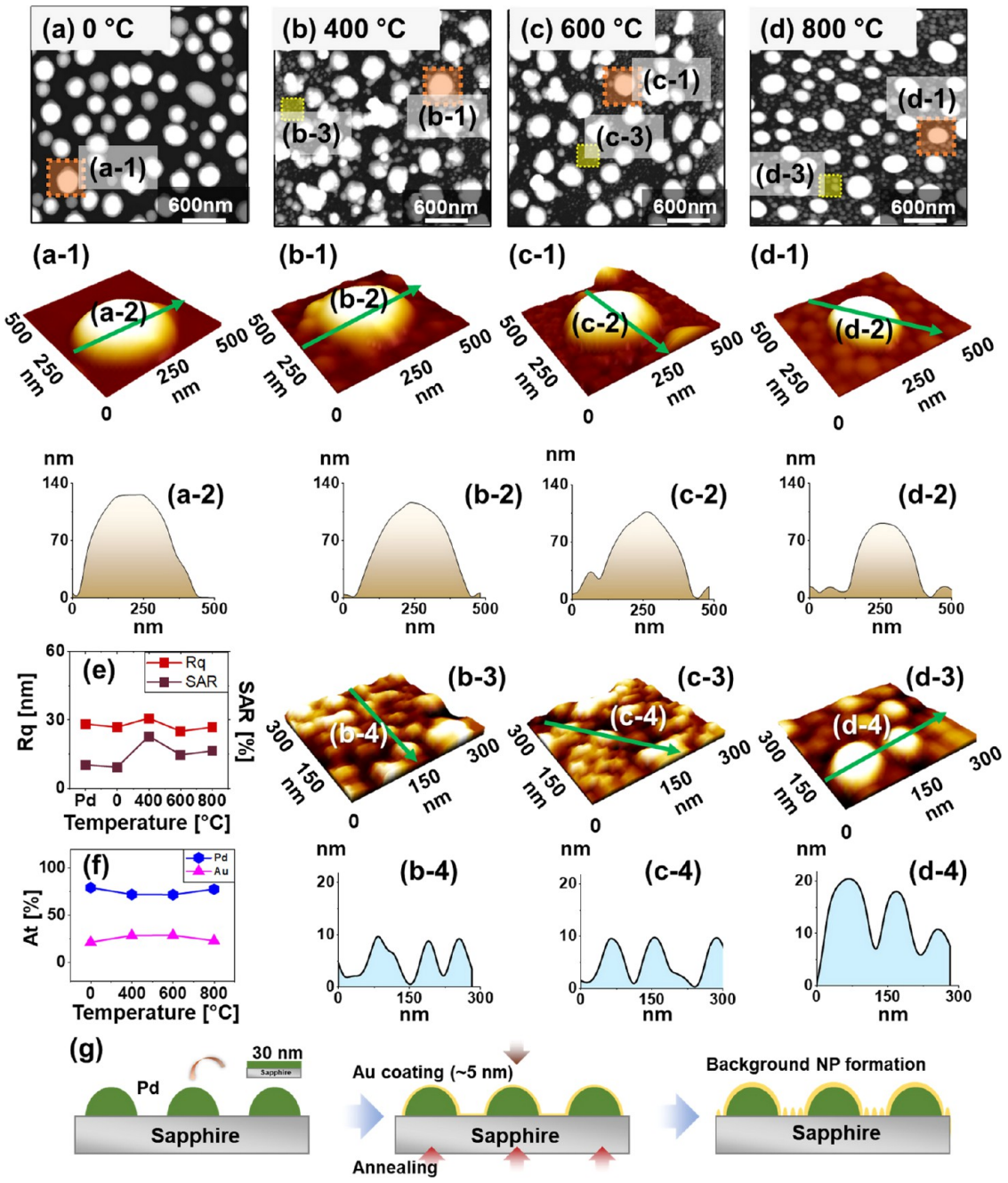

Figure 3. Evolution of core−shelled AuPd hybrid NPs by 5 nm Au coating on 30 nm Pd NP templates annealed between 0 and 800 °C. (a−d) AFM top views of 3 × 3 μm^2. ((a-1)−(d-1)) Enlarged AFM side views showing the typical core−shelled AuPd NPs. ((a-2)−(d-2)) Cross-sectional line profiles. ((b-3)−(d-3)) Enlarged side views of background Au NPs. ((b-4)−(d-4)) Cross-sectional line profiles of background Au NPs. (e) Atomic percentages of Au and Pd. (f) Summary plots of R_q and SAR. (g) Schematic of hybrid Au-shelled AuPd NPs.

nm led to the fully alloyed AuPd NPs, as shown in Figure 2. The coating thickness below 10 nm resulted in the core−shell structure with high-density small Au NPs on the background, as displayed in Figure 3. The template Pd NPs are generally stable in their original configuration even at 800 °C or higher. The presence of Pd NPs that are already in the energetically favorable configuration can provide lower-surface-energy sites, and thus, Au adatom diffusion is expected to be generally toward Pd NP sites. This will result in the formation of Au shells on Pd NPs upon annealing. Meanwhile, atomic intermixing can occur at the interface of Au and Pd.[20] When the atomic intermixing at the Au/Pd interface is intensive with a sufficient amount of Au adatoms, it can lead to the fully intermixed alloy stage. This will destroy the Pd NPs and the surface energy now will reconstruct for another optimum, resulting in a new configuration of large-alloy AuPd NPs, as shown in Figure 2. Once large AuPd NPs are formed, the preferential diffusion of adatoms toward lower-energy sites can be further enhanced, and all of the adatoms can be absorbed by the large NPs. When the degree of atomic intermixing is lower with the smaller than the critical amount of Au adatoms, the core−shell configuration can be maintained. Then, the Pd NPs are shelled by absorbing the nearby Au adatoms. At the same time, high-density small Au NPs can spontaneously form in the

https://doi.org/10.1021/acsanm.1c03748
ACS Appl. Nano Mater. XXXX, XXX, XXX−XXX

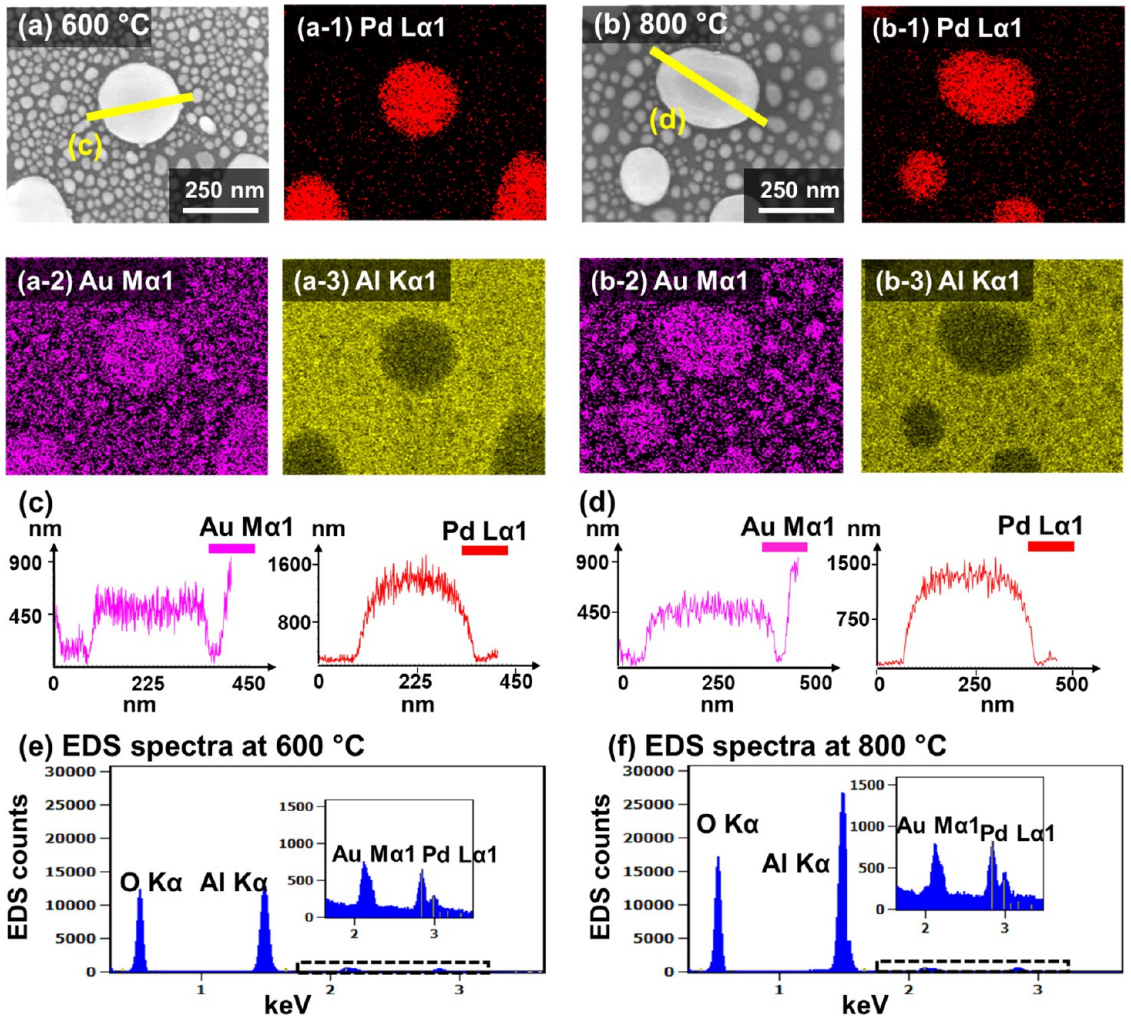

Figure 4. Elemental analysis of the core−shelled AuPd HNPs fabricated by 5 nm Au coating on the 30 nm Pd NP template at 600 and 800 °C. (a, a-3) and (b, b-3) SEM images and corresponding elemental phase maps of HNPs. (c, d) Elemental line profiles on the typical core−shelled AuPd NPs. (e, f) EDS spectra of HNPs fabricated at 600 and 800 °C.

background.[21] This can result in the formation of core−shelled AuPd hybrid NPs, as shown in Figure 3.

Figure 2 presents the surface morphology evolution of alloyed NPs fabricated by the 30 nm Au coatings on the 30 nm Pd NP templates. In this set, a distinct growth mode of bimetallic AuPd NPs was observed after the second step of SSD between 0 and 800 °C, as displayed in Figure 2a,d. Under an identical condition, the evolution of bimetallic NPs was completely distinct. Specifically, the surface morphology was fully reconstructed from the Pd NP template without background NPs, as seen in Figure 2e.[19,22] The Pd NP template covered with the thick 30 nm Au coating, i.e., 0 °C in Figure 2a, showed a similar surface morphology to the Pd NP template. When the annealing temperature was set at 400 and 600 °C, the original Pd NPs started to restructure with the intermixing of Au and Pd adatoms and somewhat interconnected nanostructures were formed, as seen in Figure 2b,c. At 800 °C, the AuPd NPs were merged, and elongated nanoclusters were formed, as shown in Figure 2d. The corresponding AFM side views and line profiles clearly demonstrate the increase in the height of alloyed AuPd NPs, as shown in Figure 2(a-1)−(d-1),(a-2)−(d-2). The RMS roughness (R_q) also reflected the increasing trend of size, as shown in Figure 2f. Meanwhile, the SAR showed similar values, which are mainly from the compensation between the increased height of nanoclusters and density reduction. Generally, R_q is more sensitive to the height change and SAR is more sensitive to the density change. The atomic percentages of Au and Pd remained constant, as seen in Figure 2g, although the surface configuration largely evolved along with the temperature. The energy-dispersive spectrometry (EDS) phase maps and the elemental line profiles demonstrated a clear match between Au and Pd at 600 and 800 °C, as shown in Figure S5. This clearly confirms the fabrication of fully alloyed AuPd nanoclusters without background Au NPs. The large-scale AFM side views and the EDS spectral analysis are presented in Figures S4 and S5. Also, the optical characterization and FDTD simulation of alloyed NPs are given in Figure S6.

Figure 3 shows the development of Au-shelled AuPd hybrid NPs (HNPs) by the 5 nm Au coating on 30 nm Pd NP templates. In general, the morphology evolution clearly demonstrates the formation of Au-shelled AuPd NPs with the high-density background Au NPs after the second phase of SSD, as shown in Figure 3a−d. With the largely reduced Au coating thickness, the degree of atomic intermixing can be significantly reduced at the Au/Pd interface. Thus, the initial Pd NPs can be retained and the preferential Au adatom

https://doi.org/10.1021/acsanm.1c03748
ACS Appl. Nano Mater. XXXX, XXX, XXX−XXX

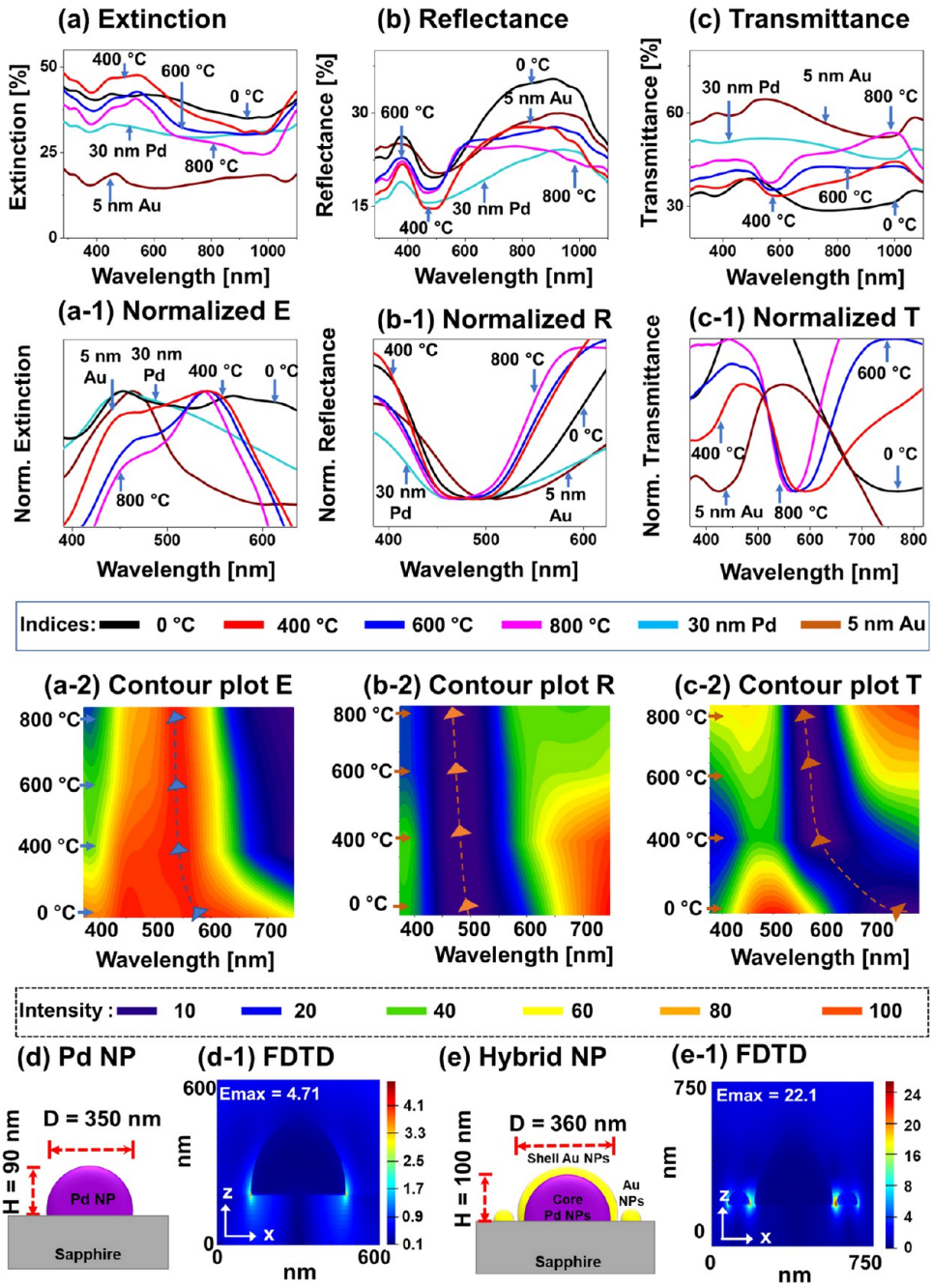

Figure 5. Optical properties of core−shelled AuPd HNP fabricated by the 5 nm Au coating on the 30 nm Pd NP template. (a−c) Extinction (E), reflectance (R), and transmittance (T) spectra in the 270−1100 nm region for the HNP, 5 nm Au on sapphire, and 30 nm Pd NP template. ((a-1)−(c-1)) Corresponding normalized and magnified spectra of peaks and dips. ((a-2)−(c-2)) Contour plots. (d, e) Schematic illustration of typical Pd NP and AuPd HNP. ((d-1), (e-1)) Corresponding side views of e-field profiles by FDTD simulations.

diffusion can result in the AuPd core−shell NP configuration. Meanwhile, the Au adatoms far away from the Pd NP absorption boundary can spontaneously form the small Au NPs in the background, as displayed in Figure 3g.[21] As the annealing temperature gradually increased, the primary NP density was comparable, as shown in Figure 3(a-1)−(d-1). However, the effective height of AuPd NPs showed a gradual reduction along with annealing likely due to the gradually increased size of background Au NPs, as shown in Figure 3(a-2)−(d-2). The average height of background Au NPs was gradually increased up to 20 nm as seen by the AFM scanning and corresponding line profiles, as shown in Figure 3(b-3)−(d-4). The R_q and SAR showed similar values ascribing from the compensation between primary NP reduction and background NP growth and these values slightly decreased at 600 and 800 °C, as shown in Figure 3e. The elemental composition also showed a similar result in Figure 3f to that in the previous set. Additional morphological and elemental analyses of hybrid Au-shelled AuPd NPs by 5 nm coating are presented in Figures S7 and S8. Also, 10 and 3 nm Au coating sets are presented in Figures S9−S11 and S14−S16. In both sets, the evolution trend of HNPs was similar to the 5 nm set with smaller background Au NPs for the 3 nm set and larger Au NPs for the 10 nm set, as clearly seen in Figures S10 and S14.

https://doi.org/10.1021/acsanm.1c03748
ACS Appl. Nano Mater. XXXX, XXX, XXX−XXX

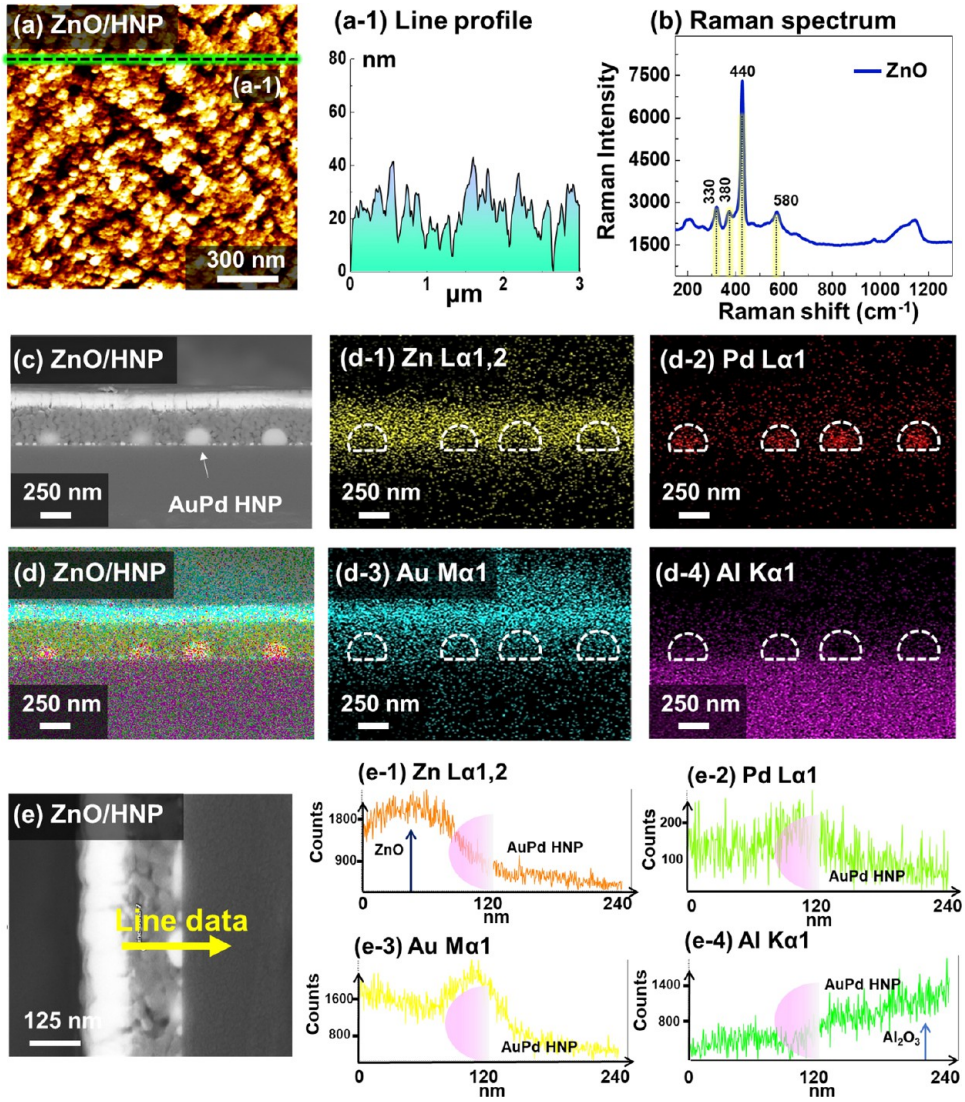

Figure 6. (a) AFM top view of ZnO/HNPs. (a-1) Corresponding line profile. (b) Raman spectrum of ZnO. (c) Cross-sectional SEM image of ZnO/HNPs. ((d)−(d-4)) Cross-sectional EDS images of ZnO/HNPs. ((e)−(e-4)) EDS line profiles of ZnO/HNPs.

Figure 4 shows the elemental analysis results for Au-shelled AuPd HNPs with 5 nm Au coating at 600 and 800 °C. The scanning electron microscopy (SEM) images in Figure 4a,b present the large core−shelled AuPd NPs surrounded by the dense smaller Au NPs. The Au NPs generally are larger at 800 °C due to enhanced surface diffusion. The Pd phase maps were seen only at the initial Pd NP sites, as demonstrated in Figure 4(a-1),(b-1), which clearly indicates that the initial Pd NPs were retained at the initial NP sites. Meanwhile, the Au phase maps showed the presence of Au throughout the surface in Figure 4(a-2),(b-2). The Au intensity was much higher on the primary NP sites due to the preferential Au adatom diffusion as discussed, which clearly indicates the formation of the Au-shelled configuration. The EDS line profiles corresponding to the yellow lines in the SEM images are presented in Figure 4c,d. Both the Pd and Au counts were detected at the primary Pd NP sites, and this also clearly suggested the formation of core−shelled AuPd NPs. Even at 800 °C, no structural deformation was observed for the primary Pd NPs after second step of SSD. Thus, the diffusion of Au atoms only led to the formation of core−shelled structure as well as the formation of high-density Au NPs. Meanwhile, the partial intermixing between Au and the outer rim of Pd NPs could occur at high temperatures due to the miscible nature of Au and Pd. However, due to the small amount of Au adatoms, the Au-shelled AuPd NPs were retained.

Figure 5 presents the optical properties of AuPd hybrid NPs fabricated with 5 nm Au sputtering onto the Pd NP template along with the extinction, reflectance, and transmittance spectra, as shown in Figure 5a−c. Generally, the Au-shelled AuPd hybrid NPs demonstrated much-improved extinction as compared to the bare Pt NPs and fully alloyed AuPd NPs. To begin with, the hybrid NPs were compared with the pure Au layer and template Pd NPs. The 5 nm Au layer showed an extinction peak in the vis region at 465 nm and a minor shoulder in the UV region at ∼330 nm.[22] Meanwhile, the fully dewetted Pd NPs in the first step of SSD exhibited the QR and DR at 330 and 450 nm, respectively. After Au coating, i.e., 0 °C, it showed a broader extinction peak in the vis region with an increment of intensity from 33 to 42%. Indeed, the vis peak can be distinguished with two minor peaks at 450 and 570 nm, which can be due to the combined effect of Au-shelled AuPd NPs and Au coating.[23] As the background Au NPs started to develop at 400 °C, the extinction peaks in the UV−vis region

https://doi.org/10.1021/acsanm.1c03748
ACS Appl. Nano Mater. XXXX, XXX, XXX−XXX

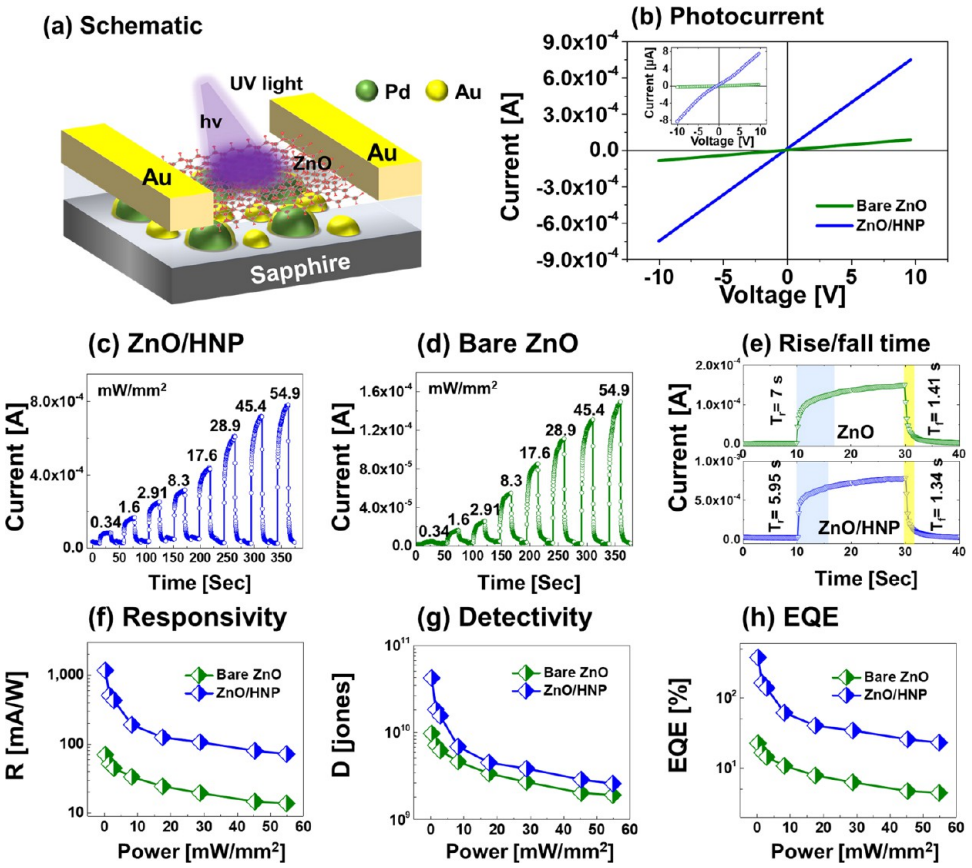

Figure 7. Photoresponse of bare ZnO and ZnO/HNP PDs under 385 nm irradiation. (a) Schematic of ZnO/HNP hybrid PDs. (b) Photocurrent of bare ZnO and ZnO/HNP PDs. The inset shows the dark current. (c) Rise/fall time. (d) and (e) Power dependency of bare ZnO and ZnO/HNP PDs at 10 V with the power density between 0.34 and 54.9 mW/mm^2. (f–h) Responsivity (R), detectivity (D), and external quantum efficiency (EQE) based on the incident power variation at 10 V.

became sharply intensified. The vis extinction peaks of each sample were normalized to visualize the LSPR trend, as shown in Figure 5(a-1). With the evolution of Au-shelled AuPd NPs and background Au NPs, the vis peaks were gradually blue-shifted from 570 nm at 0 °C to 535 nm at 800 °C, as shown in Figure 5(a-1). This can be due to the reduction in the effective height of Au-shelled AuPd NPs along with the gradual growth of background Au NPs.[19] Meanwhile, the extinction peaks showed the narrower bandwidth with high-temperature samples, which could be due to the reduced size distribution and improved uniformity of NPs,[18] as shown in a contour plot in Figure 5(a-2). In addition, the reflectance spectra in Figure 5b demonstrated clear reflectance dips, corresponding to the DR extinction peak positions. Meanwhile, the reflectance dips also followed the blue shift and reduced width of spectral peaks as in the extinction spectra in Figure 5(b-1,b-2). The transmittance spectra of AuPd hybrid NPs are displayed in Figure 5(c,c-2). The transmittance peak positions for the core–shell HNPs were also gradually blue-shifted, i.e., 770, 590, 575, and 565 nm, between 0 and 800 °C. The Au-shelled AuPd hybrid NPs fabricated with the 10 and 3 nm Au coatings showed similar trends in the optical properties, as provided in Figures S12–S17.

Figure 5d,e presents the finite-difference time-domain (FDTD) simulations of pure Pd and AuPd hybrid NPs. The electromagnetic (EM) hotspots were observed at edge positions and on the surface of pure Pd NPs, as shown in Figure 5(d-1).[23] The maximum local e-field intensity (MLEI or E_{max}) was 3.24 for the Pd NPs. The MLEI was 5.1 for the pure Au NPs, as shown in Figure S13. In the case of fully alloyed AuPd NPs, it was 8.2, as shown in Figure S6. Meanwhile, the AuPd hybrid NPs demonstrated much enhanced additional hotspots due to the high-density small Au NPs, as clearly seen in Figure 5(e-1). The MLEI was sharply increased to 26.4 due to the core–shell configuration and well-dewetted high-density background Au NPs. More detailed simulation results for the pure Pd, pure Au, and AuPd hybrid NPs are given in Figure S13.

Figure 6 shows the characterizations of the ZnO quantum dot (QD) layer deposited on the Au-shelled AuPd hybrid NPs, namely, ZnO/HNPs. The Au-shelled AuPd HNPs fabricated at 800 °C were adapted for photodetector fabrication due to the much-improved MLEI and EM hotspots, which can be beneficial for hot carrier injection. After the deposition of the ZnO QD layer, the surface became quite rough, as seen in Figure 6(a,a-1). The ZnO QD layer demonstrated the Raman bands of E_2 (high) and A_1 (LO) at 440 and 580 cm^{-1}, respectively, as seen in Figure 6b.[24] Also, the E_2 (low) mode was observed at 330 cm^{-1}. Figure 6c,e shows the cross-sectional analyses on the ZnO/HNP layer. The cross-sectional SEM image clearly showed the formation of the ZnO QD layer on the Au-shelled AuPd HNPs, as shown in Figure 6c. The ZnO QDs were clustered after spin coating and subsequent annealing. The ZnO and Pd phase maps in Figure 6(d-1,d-2) matched the SEM image well. The Au layer was slightly diffused after high-energy ion bombardment of ion milling,

https://doi.org/10.1021/acsanm.1c03748
ACS Appl. Nano Mater. XXXX, XXX, XXX–XXX

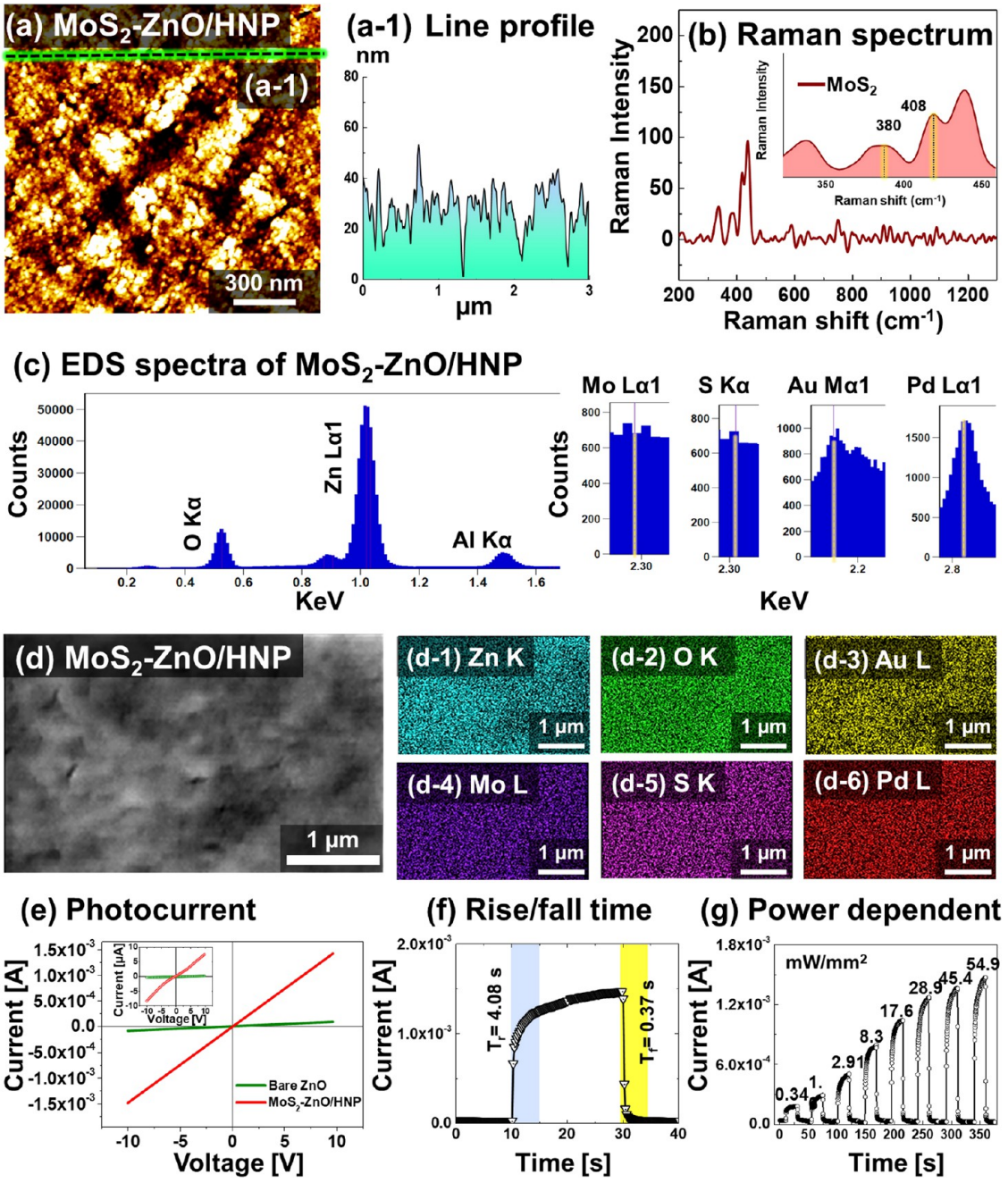

Figure 8. (a) AFM top view of the MoS2*ZnO/HNP layer. Here, MoS2*ZnO indicates the mixture in a 1:10 ratio. (a-1) Line profile of the corresponding AFM image. (b) Raman spectra of the MoS2*ZnO mixture. (c) EDS spectra of the MoS2*ZnO mixture on HNPs. ((d)−(d-6)) EDS maps of Zn, O, Au, Mo, S, and Pd. (e) Photocurrent of the MoS2*ZnO/HNP device at 54.9 mW/mm^2. The inset shows the dark current. (f) Rise/fall time of the MoS2*ZnO/HNP device. (g) Current−power characteristic at 10 V.

showing diffused Au count into the ZnO layer, as shown in Figure 6(d-3). The Al is from the sapphire (Al_2O_3) substrate, as shown in Figure 6(d-4). Similarly, the elemental line profiles on the HNPs in Figure 6(e,e-4) clearly demonstrated more than 1000 counts of each related element. The semispherical shape in the EDS line profiles indicates the AuPd hybrid nanoparticle (HNP). The high count of Zn was observed in the ZnO QD layer, as shown in Figure 6(e-1), and Pd was observed on the AuPd HNPs, as shown in Figure 6(e-2). Again, Au was observed on the ZnO QD layer up to the sapphire substrate due to diffusion by high-energy ion bombardment of ion milling, as shown in Figure 6(e-3).

Figure 7 presents the $I-V$ response of bare ZnO and ZnO/HNP photodetectors under 385 nm UV. The ZnO/HNP hybrid device was fabricated by employing the ZnO QDs and Au-shelled AuPd HNPs, as shown in Figure 7a. Figure 7b shows the current versus voltage ($I-V$) characteristics of the ZnO/HNP photodetector in comparison with those of the bare ZnO device under UV illumination (385 nm, 54.9 mW/cm^2). The dark current was 2.29×10^{-7} A for bare ZnO and 8.30×10^{-6} A for the ZnO/HNP, as shown in the inset, which showed a linear response with Ohmic contact between the ZnO QD layer and Au electrodes.[25] Upon UV illumination, the current sharply increased to 3.20×10^{-5} A for bare ZnO

https://doi.org/10.1021/acsanm.1c03748
ACS Appl. Nano Mater. XXXX, XXX, XXX−XXX

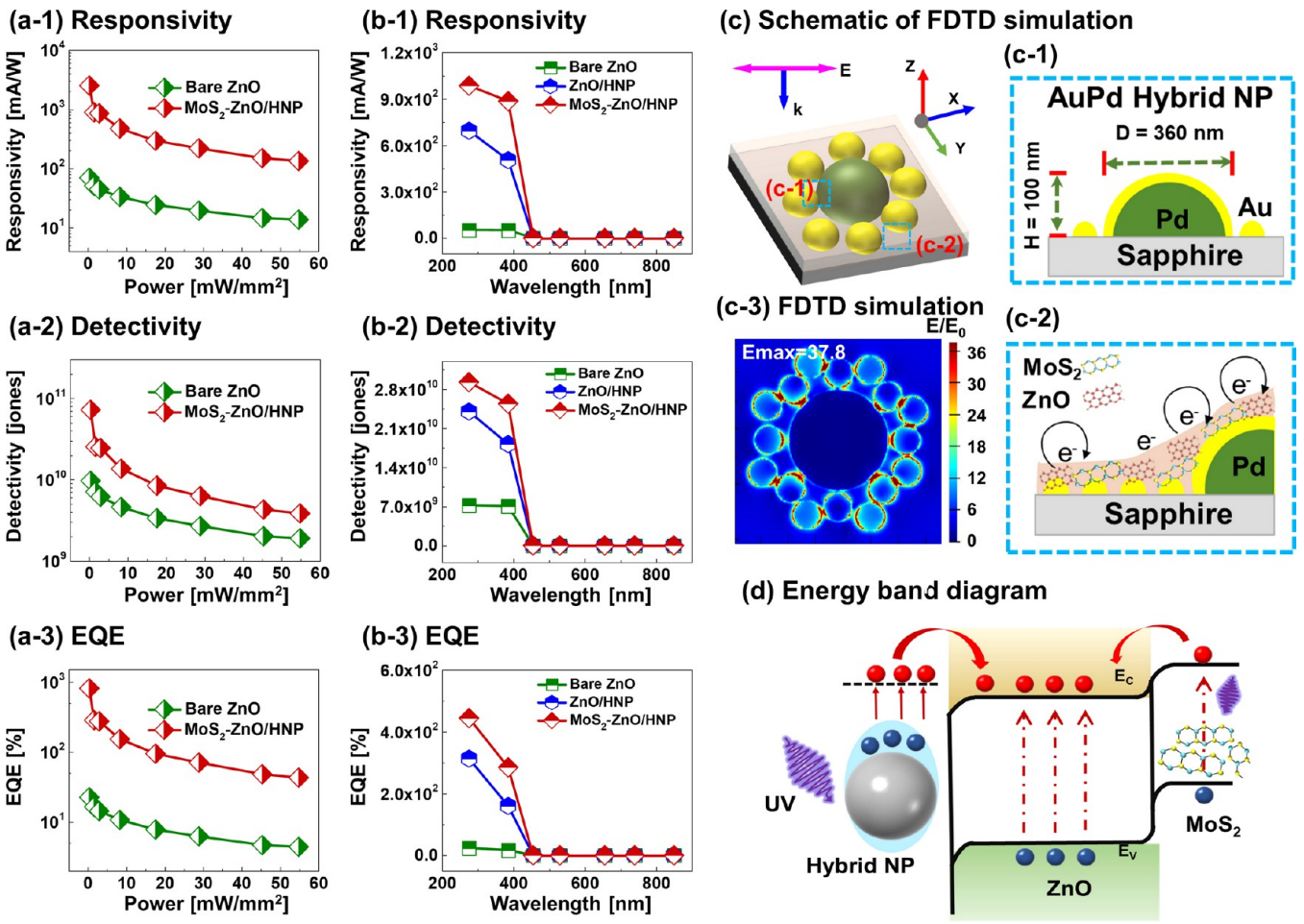

Figure 9. Photoresponse of the MoS2*ZnO/HNP hybrid PD, the FDTD simulation of MoS2*ZnO/HNP, and the photocurrent generation mechanism. ((a-1)−(a-3)) Summary plots of *R*, *D*, and EQE. ((b-1)−(b-3)) Summary plots of *R*, *D*, and EQE based on the wavelength variation at 10 V. (c) FDTD simulation of ZnO-MoS_2/HNP. (c-1) E-field distribution top view. (c-2) Schematic of AuPd HNPs with specific dimensions. (c-3) Schematic of the MoS2*ZnO mixture. (d) Energy band diagram and charge transfer process.

and reached 7.36×10^{-4} A for the ZnO/HNP. In both cases, an about two-order increase of photocurrent (I_{ph}) was observed with a much higher I_{ph} for the ZnO/HNP device. This clearly shows that the incorporation of Au-shelled AuPd HNPs into the photodetector matrix resulted in a significant increase of photocurrent (I_{ph}) due to the increased photocarrier injection by the Au-shelled AuPd HNPs.[26] Further, the UV excitation power was varied from 0.34 to 54.9 mW/mm^2 at 10 V, as seen in Figure 7c,d. The increase in the I_{ph} with the gradually increased incident power at a fixed bias can be due to more excitation of carriers, which confirms that the ZnO QD layer is of good quality.[25] In terms of the rise (t_r) and fall time (t_f), while the bare ZnO showed t_r = 7 s and t_f = 1.41 s, the ZnO/HNP demonstrated improved values of t_r = 5.95 s and t_f = 1.34. These are quite good numbers for the ZnO-based photodetectors. Further, the performance parameters such as responsivity (R), detectivity (D), and external quantum efficiency (EQE) were evaluated for the ZnO/HNP and bare ZnO devices based on the following equations: $R = \frac{I_{ph} - I_d}{P_d \times A}$, $D = \frac{R \cdot A^{1/2}}{(2qI_d)^{1/2}}$, and $\mathrm{EQE} = R \times \frac{1240}{\lambda} \times 100\%$, where I_{ph} and I_d are photo and dark currents and P_d is the power density. A is the photoactive area, q is the elementary charge, and λ is the wavelength of light in nm.[27,28] A photoresponsivity of 1,166.8 mA/W was obtained in the ZnO/HNP photodetector at 0.34 mW/mm^2, and that of bare ZnO was 69.4 mA/W in Figure 7f. This shows that the ZnO/HNP device demonstrated about 17 times higher photoresponsivity. The photoresponsivity was generally high at low power due to the saturation of photocarrier generation.[29] Accordingly, the ZnO/HNP demonstrated much-improved detectivity and EQE of 4.20×10^{10} jones and 375%, respectively, at 0.34 mW/mm^2, as seen in Figure 7g,h. The bare ZnO device demonstrated a detectivity and EQE of 9.64×10^9 jones and 22.36%, respectively, at 0.34 mW/mm^2. The specific numerical values of *R*, *D*, and EQW at different illumination powers are summarized in Table S1.

Figure 8 shows the mixed MoS_2*ZnO application on the Au-shelled AuPd hybrid NPs, namely, the MoS_2*ZnO/HNP device. Here, the MoS_2 nanoflakes and ZnO quantum dots (QDs) were mixed in a 1:10 ratio from the solutions in Figure S18 and spin-coated and annealed on the AuPd HNPs as in the ZnO/HNP application. The mixture ratio of 10:1 was determined based on the SERS study of the mixture of methylene blue (MB) and MoS_2 nanoplatelets.[30] The MoS_2 NFs are 2-D transition-metal dichalcogenide (TMD) semiconductors that offer added photocarriers to the device matrix. The surface morphology became slightly rougher, as seen in Figure 8(a,a-1), than that of the bare ZnO. After the addition of 2-D MoS_2 nanoflakes, the E_{2g}^1 and A_{1g} phonon modes

https://doi.org/10.1021/acsanm.1c03748
ACS Appl. Nano Mater. XXXX, XXX, XXX−XXX

Table 1. Performance Comparison of the ZnO-Related Photodetectors in the UV Region with Various Materials[a]

material	bias (V)	light source (nm)	R (mA/W)	D (jones)	EQE (%)	t_r (s)	t_f (s)
ZnO/NiO[45]	0	350	0.415			7.5	4.8
$Mg_yZn_{1-y}O$/ZnO[46]	5	365	160				
ZnO/graphene nanodots[47]	5	360	22.55		9.32		
ZnO/GaN[48]	1	360	225	4.83×10^{13}			
ZnO/$CuCrO_2$[49]	0	365	3.43				
Al/ZnO[50]	10	365	11 976.45		4068.71	2.17	0.48
ZnO/GQD thin film[51]	−3		560	2.1×10^{11}		0.37	0.78
Au NPs/ZnO[52]	2	375	126 000			<0.5	<0.5
PbS/ZnO[53]	5	375	4540	3.98×10^{12}			
perovskite/ZnO[54]	0	300	48	4.5×10^{11}		0.014	0.012
ZnO/ZnS[55]	3	365	173.5	1.5×10^{13}		21.3	42
MoS_2*ZnO/HNP	**10**	**385**	**2525.77**	**7.25×10^{11}**	**813.49**	**4.08**	**0.37**

[a]The last material configuration in bold is for the device demonstrated in this work.

appeared at 380 and 408 cm^{-1}, respectively, as shown in Figure 8b.[31,32] The EDS spectra demonstrated all of the elemental peaks in the MoS_2*ZnO/HNP layer, i.e., Zn, O, Au, Mo, S, and Pd, in Figure 8c. Similarly, the EDS maps showed the presence of all of the elements, i.e., Zn, O, Au, Mo, S, and Pd, of the MoS_2*ZnO/HNP device in Figure 8d. Upon UV illumination of the MoS_2*ZnO/HNP device, generally, the photocurrent characteristics were further improved as compared to the ZnO/HNP device. The dark current was 8.58×10^{-6} A, as shown in the inset in Figure 8e, about an order higher as compared to that of bare ZnO device of 3.39×10^{-7} A and had a similar value to that of ZnO/HNP of 8.30×10^{-6} A. The photocurrent (I_{ph}) was sharply increased to 1.49×10^{-3} A under a power density of 54.9 mW/mm^2 at 10 V. It was 3.20×10^{-5} A for bare ZnO and 7.36×10^{-4} A for the ZnO/HNP at the same condition. Clearly, the addition of MoS_2 nanoflakes further increased the I_{ph}, which can be attributed to the increased electron−hole generation and increased mobility of photogenerated carriers with the addition of MoS_2 NFs.[28,29] The rise (t_r) and fall (t_f) times were also improved to 4.08 and 0.37 s, respectively, with the addition of MoS_2 nanoflakes, as seen in Figure 8f. With the bias, the UV excited photocarriers can be quickly collected through the electrodes due to the increased drift velocity of carriers.[33,34] Also, the I_{ph} over various power densities showed a gradual increase and this confirmed that the mixed MoS_2*ZnO layer is a good quality of the active channel and can offer improved photoresponse.

The responsivity (R), detectivity (D), and external quantum efficiency (EQE) of MoS_2*ZnO/HNP are summarized in Figure 9(a-1)−(a-3) compared with those of the ZnO device. MoS_2*ZnO/HNP demonstrated the highest maximum photoresponsivity of 2525 mA/W at 0.34 mW/mm^2, which is more than 36 times greater than that of the bare ZnO device of 69.4 mA/W. Accordingly, MoS_2*ZnO/HNP demonstrated a much-improved detectivity and EQE of 7.25×10^{11} jones and 813% at 0.34 mW/mm^2, respectively, as seen in Figure 9(a-2)−9(a-3). In addition, the performance parameters were tested at various wavelengths ranging from the UV to NIR between 275 and 850 nm at a fixed power of 1.6 mW/mm^2, as shown in Figure 9(b-1)−(b-3). The MoS_2*ZnO/HNP device exclusively responded to the UV illumination and all other regions showed near-zero values, indicating that the MoS_2*ZnO/HNP photodetector shows good selectivity for the UV region. Overall, the MoS_2*ZnO/HNP device presented the best performance with a high photocurrent of 1.49×10^{-3} A along with the improved rise (t_r) and fall (t_f) times. Table 1 summarizes the performance comparison of the ZnO-related photodetectors in the UV region with various materials, and the MoS_2*ZnO/HNP device presents one of the best performances. The current−time characteristics of various devices at different wavelength illuminations are given in Figures S20 and S21, and the specific numerical values at different illumination powers are summarized in Tables S2 and S3.

Figure 9c shows the local e-field distribution of the hybrid configuration via FDTD simulations. A mixed layer of MoS_2 nanoflakes and ZnO QDs was applied on the Au-shelled AuPd hybrid NPs, as shown in Figure 9(c-1,c-2). With the application of the mixed layer of MoS_2*ZnO, the maximum local e-field intensity (MLEI) was sharply increased to 64.25, as shown in Figure 9(c-3), which can be compared with the MLEI of 30.83 of AuPd hybrid NPs. The MLEI was over twice increased after the addition of MoS_2 nanoflakes and ZnO QDs. Also, much enhanced hotspots were observed around the HNPs. Especially, the small high-density Au NPs contributed a lot to the hotspot enhancement. This clearly shows that the hybrid system of MoS_2/ZnO/HNP can significantly improve the hotspots and LSPR with a much higher local e-field distribution. Figure 9d shows the band diagram of the MoS_2*ZnO/HNP hybrid configuration, which explains the photocurrent (I_{ph}) enhancement mechanism. The improved photocurrent can be attributed to the increased photocarrier injection first by the Au-shelled AuPd hybrid NPs and then by the addition of MoS_2 nanoflakes. The optical band gap of ZnO QDs is ∼3.34 eV, and thus, ZnO QDs can effectively absorb the UV photons. The electron−hole pairs generated in the direct band gap of the ZnO QD layer are responsible for the I_{ph} of 3.20×10^{-5} A, as shown in Figure 7b. Then, along with the incorporation of Au-shelled AuPd hybrid NPs, the I_{ph} was sharply increased to 7.36×10^{-4} A for the ZnO/HNP, as shown in Figure 7b. In the presence of AuPd hybrid NPs, the plasmon-meditated hot carriers can contribute to the increased I_{ph} due to the injection of energetic hot carriers induced by the LSPR of AuPd hybrid NPs, as shown in Figure 9d. The work function of ZnO is ∼5.3 eV, which is slightly higher than that of Au (5.1 eV) or Pd (5.12 eV). Thus, a downward band bending can occur between the AuPd hybrid NPs and ZnO QD layers.[35,36] The alloy materials' work function is generally in between the two work functions depending on the composition, and when the metal working function is smaller, it generally results in the Ohmic contact.[36] The hot carriers generated by the strong LSPR of Au-shelled AuPd hybrid NPs

https://doi.org/10.1021/acsanm.1c03748
ACS Appl. Nano Mater. XXXX, XXX, XXX−XXX

can be effectively collected to the conduction band of ZnO as the ZnO QDs are fully surrounding the AuPd hybrid NPs. Finally, the I_{ph} was again largely increased to 1.49×10^{-3} A for the MoS_2*ZnO/HNP, as seen in Figure 8e, with the incorporation of MoS_2 nanoflakes. The band gap of MoS_2 nanoflakes is 1.5−1.9 eV, and thus, the photocarriers can be spontaneously generated upon UV illumination and photon absorption.[37−39] The MoS_2 NFs are 2-D layered TMD semiconductors, which can effectively absorb the higher-energy photons and thus can contribute additional photocarriers to the device matrix. The overall photocurrent and response speed can be significantly improved with the additive contribution of photogenerated carriers from the Au-shelled AuPd hybrid NPs and MoS_2 nanoflakes in the MoS_2*ZnO/HNP hybrid device.[40,41] This clearly shows that the mixed application of MoS_2 NFs and ZnO QDs on the Au-shelled AuPd hybrid NPs, namely, the MoS_2*ZnO/HNP hybrid photodetector configuration, can significantly improve the photodetector characteristics and thus can offer a useful hybrid photodetector configuration by utilizing the increased hot carriers due to the LSPR and photocarrier injection.

CONCLUSIONS

In conclusion, a two-step SSD method was utilized to fabricate fully alloyed AuPd NPs and core−shelled AuPd hybrid NPs. The alloyed NPs were fabricated with the Au coating thickness above 30 nm, and the core−shelled AuPd hybrid NPs were formed below 10 nm. Starting from the identical Pd platform, totally different configurations of AuPd NPs resulted due to the variation in the atomic intermixing degree and preferential Au adatom diffusion. Subsequently, the surface energy reconstruction and spontaneous background Au NP formation played the main role in the determination of the final AuPd NP configuration. The Au-shelled AuPd hybrid NPs with the 5 nm Au coating at 800 °C were adapted for photodetector fabrication based on the optical analyses and FDTD simulations. The mixed application of MoS_2 nanoflakes and ZnO QDs on the Au-shelled AuPd hybrid NPs, i.e., the MoS_2*ZnO/HNP configuration, demonstrated the best photocurrent of 1.49×10^{-3} A with the improved t_r = 4.08 s and t_f = 0.37 s. Accordingly, the superior photoresponsivity of 2,525 mA/W, detectivity of 7.251×10^{11} jones, and EQE of 813% at 0.34 mW/mm^2 were observed. The enhanced performance was attributed to the increased photocarrier injection and sufficient electron collection by the MoS_2*ZnO/HNP configuration.

EXPERIMENTAL METHODS

Sample Preparation and NP Fabrication. In this work, the sapphire (0001) wafer was used as the substrate for the NP and photodetector fabrication. First, the sapphire substrates were degassed in a vacuum chamber.[30] The morphology and optical characterizations of degassed sapphire are provided in Figure S1. Various films were deposited on the substrates using plasma-assisted sputtering under a base pressure below 1×10^{-1} torr at an ionization current of 3 mA. The fabrication of alloyed AuPd and hybrid NPs involved a two-step SSD. In the first step of SSD, the 30 nm Pd film was deposited and annealed at 800 °C for 450 s to fabricate the Pd NP templates. Then, the Au films of 3, 5, 10, and 30 nm were deposited on the Pd NP templates. In the second step, the Au-coated samples were annealed at each target temperature of 400, 600, and 800 °C for 120 s. The postannealing process was controlled in the PLD chamber under 1×10^{-4} torr at a ramp rate of 4 °C/s.

ZnO Quantum Dot (QD) and MoS_2 Nanoflake (NF) Preparation. The ZnO QD solution was prepared by a chemical synthesis method.[42] The mixture solvent of chloroform (4 mL) and methanol (2 mL) was used to disperse the remaining product by ultrasonication for 5 min, as seen in Figure S18a. The molybdenum disulfide (MoS_2) nanoflakes were about a few hundred nanometers in diameter with fewer atomic layers in the powder form. The molybdenum disulfide (MoS_2) nanoflake solution was prepared by dissolving 0.25 mg of MoS_2 nanoflakes in 1 mL of ethanol. Before the application, the MoS_2 nanoflake solution was ultrasonicated for 10 min to improve the dispersion, as seen in Figure S18b.

Photodetector Fabrication and FDTD Simulation. The bare ZnO device was fabricated by spin coating of the as-prepared ZnO QDs at 2000 rpm for 30 s on sapphire. The spin coating process was repeated 5 times to form appropriately uniform QD or mixture layers. Similarly, the ZnO/HNP device was fabricated by spin coating of ZnO QD layers on the core−shelled AuPd hybrid NPs. In the case of the MoS_2*ZnO/HNP device, the ZnO QDs and MoS_2 NPs were mixed in 10:1 ratio and spin-coated on the core−shelled AuPd HNPs. After deposition, the samples were annealed in the PLD chamber at three different stages such as 100 °C for 10 min in vacuum, 300 °C for 10 min under the 10 mL O_2 flow, and 550 °C for 1 h under the 20 mL O_2 flow. Finally, a pair of Au electrodes having a 200 μm gap and 100 nm thickness was deposited using plasma-assisted sputtering on a shadow mask. The simulations of e-field distributions for the various types of NPs, ZnO quantum QDs, and MoS_2 NFs on the HNPs were performed by finite-difference time-domain (FDTD) (Lumerical, Canada). The dielectric constants were referenced from the Palik and Palm models[43,44] for the Au and Pd and from the Query and Beal and Hughes models[31,32] for the ZnO QDs and MoS_2 NFs. The dielectric constant of alloy NPs was averaged based on their atomic percentages. More details on the simulation and characterization section with the frequently utilized equipment are given in the Supplementary materials.

ASSOCIATED CONTENT

Supporting Information

The Supporting Information is available free of charge at https://pubs.acs.org/doi/10.1021/acsanm.1c03748.

Additional morphological, elemental, optical, and electrical characterizations of bare sapphire, AuPd HNPs, various photoreactors including the AFM images, SEM images, EDS spectra, optical spectra, FDTD simulations, and *IV* responses (Figures S1−S21) (PDF)

AUTHOR INFORMATION

Corresponding Authors

Sundar Kunwar − *Center for Integrated Nanotechnologies (CINT), Los Alamos National Laboratory, Los Alamos, New Mexico 87545, United States*; Email: sundar@lanl.gov

Jihoon Lee − *Department of Electronic Engineering, College of Electronics and Information, Kwangwoon University, Seoul 01897, Republic of Korea*; orcid.org/0000-0002-0508-486X; Email: jihoonlee@kw.ac.kr

Authors

Shusen Lin − *Department of Electronic Engineering, College of Electronics and Information, Kwangwoon University, Seoul 01897, Republic of Korea*; orcid.org/0000-0002-7121-4431

Rutuja Mandavkar − *Department of Electronic Engineering, College of Electronics and Information, Kwangwoon University, Seoul 01897, Republic of Korea*; orcid.org/0000-0002-9706-876X

Rakesh Kulkarni − *Department of Electronic Engineering, College of Electronics and Information, Kwangwoon*

https://doi.org/10.1021/acsanm.1c03748
ACS Appl. Nano Mater. XXXX, XXX, XXX−XXX

University, Seoul 01897, Republic of Korea; orcid.org/0000-0002-5119-2693

Shalmali Burse − *Department of Electronic Engineering, College of Electronics and Information, Kwangwoon University, Seoul 01897, Republic of Korea*

Md Ahasan Habib − *Department of Electronic Engineering, College of Electronics and Information, Kwangwoon University, Seoul 01897, Republic of Korea;* orcid.org/0000-0002-9738-1721

So Hee Kim − *Advanced Analysis Center, Korea Institute of Science and Technology (KIST), Seoul 02792, Republic of Korea*

Ming-Yu Li − *School of Science, Wuhan University of Technology, Wuhan, Hubei 430070, China;* orcid.org/0000-0003-4812-8604

Complete contact information is available at: https://pubs.acs.org/10.1021/acsanm.1c03748

Notes

The authors declare no competing financial interest.

■ ACKNOWLEDGMENTS

Financial support from the National Research Foundation of Korea (NRF-2018R1A6A1A03025242 and no. NRF-2019R1A2C4069438), the National Natural Science Foundation of China (61705070), the NNSA's Laboratory Directed Research and Development Program of USA (89233218CNA000001), and the research grant of Kwangwoon University in 2022 is gratefully acknowledged. Gyu Min Hwang from the Korea Institute of Science and Technology (KIST) is thankfully acknowledged for ion milling.

■ REFERENCES

(1) An, J.; Le, T. S. D.; Lim, C. H. J.; Tran, V. T.; Zhan, Z.; Gao, Y.; Zheng, L.; Sun, G.; Kim, Y. J. Single-Step Selective Laser Writing of Flexible Photodetectors for Wearable Optoelectronics. *Adv. Sci.* **2018**, *5*, No. 1800496.

(2) Gao, S.; Hao, S.; Huang, Z.; Yuan, Y.; Han, S.; Lei, L.; Zhang, X.; Shahbazian-Yassar, R.; Lu, J. Synthesis of High-Entropy Alloy Nanoparticles on Supports by the Fast Moving Bed Pyrolysis. *Nat. Commun.* **2020**, *11*, No. 2016.

(3) Sohrabi Kashani, A.; Piekny, A.; Packirisamy, M. Using Intracellular Plasmonics to Characterize Nanomorphology in Human Cells. *Microsyst. Nanoeng.* **2020**, *6*, No. 110.

(4) Yang, L.; Yang, Q.; Hu, J.; Bao, Z.; Su, B.; Zhang, Z.; Ren, Q.; Xing, H. Metal Nanoparticles in Ionic Liquid-Cosolvent Biphasic Systems as Active Catalysts for Acetylene Hydrochlorination. *AIChE J.* **2018**, *64*, 2536−2544.

(5) Mitchell, M. J.; Billingsley, M. M.; Haley, R. M.; Wechsler, M. E.; Peppas, N. A.; Langer, R. Engineering Precision Nanoparticles for Drug Delivery. *Nat. Rev. Drug Discovery* **2021**, *20*, 101−124.

(6) Dubey, A.; Mishra, R.; Hsieh, Y. H.; Cheng, C. W.; Wu, B. H.; Chen, L. J.; Gwo, S.; Yen, T. J. Aluminum Plasmonics Enriched Ultraviolet GaN Photodetector with Ultrahigh Responsivity, Detectivity, and Broad Bandwidth. *Adv. Sci.* **2020**, *7*, No. 2002274.

(7) Karaagac, H.; Erdal Aygun, L.; Parlak, M.; Ghaffari, M.; Biyikli, N.; Kemal Okyay, A. Au/TiO 2 Nanorod-Based Schottky-Type UV Photodetectors. *Phys. Status Solidi RRL* **2012**, *6*, 442−444.

(8) Zhang, Y.; Zhao, X.; Chen, J.; Li, S.; Yang, W.; Fang, X. Self-polarized BaTiO3 for Greatly Enhanced Performance of ZnO UV Photodetector by Regulating the Distribution of Electron Concentration. *Adv. Funct. Mater.* **2020**, *30*, No. 1907650.

(9) Lee, K. S.; Park, Y. J.; Shim, J.; Chung, H.-S.; Yim, S.-Y.; Hwang, J. Y.; Cho, H.; Lim, B.; Son, D. I. ZnO@ Graphene QDs with Tuned Surface Functionalities Formed on Eco-Friendly Keratin Nanofiber Textile for Transparent and Flexible Ultraviolet Photodetectors. *Org. Electron.* **2020**, *77*, No. 105489.

(10) Mandavkar, R.; Kulkarni, R.; Lin, S.; Pandit, S.; Burse, S.; Ahasan Habib, M.; Pandey, P.; Hee Kim, S.; Li, M.-Y.; Kunwar, S.; Lee, J. Significantly Improved Photo Carrier Injection by the MoS2/ZnO/HNP Hybrid UV Photodetector Architecture. *Appl. Surf. Sci.* **2021**, No. 151739.

(11) Kunwar, S.; Pandey, P.; Pandit, S.; Sui, M.; Lee, J. Tunable Localized Surface Plasmon Resonance by Self-Assembly of Trimetallic and Bimetallic Alloy Nanoparticles via Ag Sublimation from Ag/Au/Pt Tri-Layers. *Appl. Surf. Sci.* **2020**, *504*, No. 144545.

(12) Kunwar, S.; Pandit, S.; Jeong, J. H.; Lee, J. Improved Photoresponse of UV Photodetectors by the Incorporation of Plasmonic Nanoparticles on GaN Through the Resonant Coupling of Localized Surface Plasmon Resonance. *Nano-Micro Lett.* **2020**, *12*, No. 91.

(13) Borah, R.; Verbruggen, S. W. Silver−Gold Bimetallic Alloy versus Core−Shell Nanoparticles: Implications for Plasmonic Enhancement and Photothermal Applications. *J. Phys. Chem. C* **2020**, *124*, 12081−12094.

(14) Jeong, J.-H.; Kunwar, S.; Pandit, S.; Lee, J. CoP2 Nanoparticles Deposited on Nanometer-Thick Pt-Coated Fluorine-Doped Tin Oxide Substrates as Electrocatalysts for Simultaneous Hydrogen Evolution and Oxygen Evolution. *ACS Appl. Nano Mater.* **2020**, *3*, 6507−6515.

(15) Brongersma, M. L.; Halas, N. J.; Nordlander, P. Plasmon-Induced Hot Carrier Science and Technology. *Nat. Nanotechnol.* **2015**, *10*, 25−34.

(16) Pandit, S.; Kunwar, S.; Kulkarni, R.; Mandavka, R.; Lin, S.; Lee, J. Applied Surface Science Fabrication of Hybrid Pd @ Ag Core-Shell and Fully Alloyed Bi-Metallic AgPd NPs and SERS Enhancement of Rhodamine 6G by a Unique Mixture Approach with Graphene Quantum Dots. *Appl. Surf. Sci.* **2021**, *548*, No. 149252.

(17) Huang, J.; Kim, F.; Tao, A. R.; Connor, S.; Yang, P. Spontaneous Formation of Nanoparticle Stripe Patterns through Dewetting. *Nat. Mater.* **2005**, *4*, 896−900.

(18) Zhan, Z.; Xu, R.; Mi, Y.; Zhao, H.; Lei, Y. Highly Controllable Surface Plasmon Resonance Property by Heights of Ordered Nanoparticle Arrays Fabricated via a Nonlithographic Route. *ACS Nano* **2015**, *9*, 4583−4590.

(19) Kunwar, S.; Pandey, P.; Lee, J. Enhanced Localized Surface Plasmon Resonance of Fully Alloyed AgAuPdPt, AgAuPt, AuPt, AgPt, and Pt Nanocrystals: Systematical Investigation on the Morphological and LSPR Properties of Mono -, Bi-, Tri-, and Quad-Metallic Nanoparticles. *ACS Omega* **2019**, *4*, 17340−17351.

(20) Magogodi, S.; Mtshali, C.; Halindintwali, S.; Khumalo, Z.; Mongwaketsi, N.; Cloete, K.; Madito, M.; Pieters, C.; Sook, A.; Mc Donald, E.; Cummings, F.; Arendse, C. Effect of the Annealing Atmosphere on the Layer Interdiffusion in Pd/Ti/Pd Multilayer Stacks Deposited on Pure Ti and Ti-Alloy Substrates. *Nucl. Instrum. Methods Phys. Res., Sect. B* **2019**, *461*, 37−43.

(21) Altomare, M.; Nguyen, N. T.; Schmuki, P. Templated Dewetting: Designing Entirely Self-Organized Platforms for Photocatalysis. *Chem. Sci.* **2016**, *7*, 6865−6886.

(22) Romani, E. C.; Vitoreti, D.; Gouvêa, P. M. P.; Caldas, P. G.; Prioli, R.; Paciornik, S.; Fokine, M.; Braga, A. M. B.; Gomes, A. S. L.; Carvalho, I. C. S. Gold Nanoparticles on the Surface of Soda-Lime Glass: Morphological, Linear and Nonlinear Optical Characterization. *Opt. Express* **2012**, *20*, 5429−5439.

(23) Kvitek, O.; Havelka, V.; Vesely, M.; Reznickova, A.; Svorcik, V. Preparation of Alloyed and "Core-Shell" Au/Ag Bimetallic Nanostructures on Glass Substrate by Solid State Dewetting. *J. Alloys Compd.* **2020**, *829*, No. 154627.

(24) Zhan, Z.; Zheng, L.; Pan, Y.; Sun, G.; Li, L. Self-Powered, Visible-Light Photodetector Based on Thermally Reduced Graphene Oxide−ZnO (RGO−ZnO) Hybrid Nanostructure. *J. Mater. Chem.* **2012**, *22*, 2589−2595.

(25) Wang, P.; Wang, Y.; Ye, L.; Wu, M.; Xie, R.; Wang, X.; Chen, X.; Fan, Z.; Wang, J.; Hu, W. Ferroelectric Localized Field−Enhanced

ZnO Nanosheet Ultraviolet Photodetector with High Sensitivity and Low Dark Current. *Small* **2018**, *14*, No. 1800492.
(26) Pak, Y.; Mitra, S.; Alaal, N.; Xin, B.; Lopatin, S.; Almalawi, D.; Min, J.-W.; Kim, H.; Kim, W.; Jung, G.-Y.; Roqan, I. S. Dark-Current Reduction Accompanied Photocurrent Enhancement in p-Type MnO Quantum-Dot Decorated n-Type 2D-MoS2-Based Photodetector. *Appl. Phys. Lett.* **2020**, *116*, No. 112102.
(27) Sun, B.; Wang, Z.; Liu, Z.; Tan, X.; Liu, X.; Shi, T.; Zhou, J.; Liao, G. Tailoring of Silver Nanocubes with Optimized Localized Surface Plasmon in a Gap Mode for a Flexible MoS2 Photodetector. *Adv. Funct. Mater.* **2019**, *29*, No. 1900541.
(28) Lu, J.; Zheng, Z.; Yao, J.; Gao, W.; Zhao, Y.; Xiao, Y.; Li, J. 2D In2S3 Nanoflake Coupled with Graphene toward High-Sensitivity and Fast-Response Bulk-Silicon Schottky Photodetector. *Small* **2019**, *15*, No. 1904912.
(29) Liu, Y.; Zhang, Y.; Zhao, K.; Yang, Z.; Feng, J.; Zhang, X.; Wang, K.; Meng, L.; Ye, H.; Liu, M.; Liu, S. Frank. A 1300 Mm2 Ultrahigh-Performance Digital Imaging Assembly Using High-Quality Perovskite Single Crystals. *Adv. Mater.* **2018**, *30*, No. 1707314.
(30) Lin, S.; Mandavkar, R.; Kulkarni, R.; Pandit, S.; Burse, S.; Habib, M. A.; Kunwar, S.; Lee, J. Hybridization of 2D MoS2 Nanoplatelets and PtAu Hybrid Nanoparticles for the SERS Enhancement of Methylene Blue. *Adv. Mater. Interfaces* **2021**, *8*, 1−13.
(31) Kumar, A.; Ahluwalia, P. K. A First Principle Comparative Study of Electronic and Optical Properties of 1H−MoS2 and 2H−MoS2. *Mater. Chem. Phys.* **2012**, *135*, 755−761.
(32) Theiss, S.; Voggel, M.; Kuper, H.; Hoermann, M.; Krings, U.; Baum, P.; Becker, J. A.; Wittmann, V.; Polarz, S. Ligand-Programmed Consecutive Symmetry Break(s) in Nanoparticle Based Materials Showing Emergent Phenomena: Transitioning from Sixfold to Threefold Symmetry in Anisotropic ZnO Colloids. *Adv. Funct. Mater.* **2021**, *31*, No. 2009104.
(33) Deka Boruah, B. Zinc Oxide Ultraviolet Photodetectors: Rapid Progress from Conventional to Self-Powered Photodetectors. *Nanoscale Adv.* **2019**, *1*, 2059−2085.
(34) Liu, L.; Zhai, T. Wafer-scale Vertical van Der Waals Heterostructures. *InfoMat* **2021**, *3*, 3−21.
(35) Nie, Z.; Shi, Y.; Qin, S.; Wang, Y.; Jiang, H.; Zheng, Q.; Cui, Y.; Meng, Y.; Song, F.; Wang, X.; Turcu, I. C. E.; Wang, X.; Xu, Y.; Shi, Y.; Zhao, J.; Zhang, R.; Wang, F. Tailoring Exciton Dynamics of Monolayer Transition Metal Dichalcogenides by Interfacial Electron-Phonon Coupling. *Commun. Phys.* **2019**, *2*, No. 103.
(36) Kwak, D.; Lei, Y.; Maric, R. Ammonia Gas Sensors: A Comprehensive Review. *Talanta* **2019**, *204*, 713−730.
(37) Kim, K. S.; Ji, Y. J.; Kim, K. H.; Choi, S.; Kang, D. H.; Heo, K.; Cho, S.; Yim, S.; Lee, S.; Park, J. H.; Jung, Y. S.; Yeom, G. Y. Ultrasensitive MoS2 Photodetector by Serial Nano-Bridge Multi-Heterojunction. *Nat. Commun.* **2019**, *10*, No. 4701.
(38) Long, M.; Wang, Y.; Wang, P.; Zhou, X.; Xia, H.; Luo, C.; Huang, S.; Zhang, G.; Yan, H.; Fan, Z.; Wu, X.; Chen, X.; Lu, W.; Hu, W. Palladium Diselenide Long-Wavelength Infrared Photodetector with High Sensitivity and Stability. *ACS Nano* **2019**, *13*, 2511−2519.
(39) Shi, J.; Zhu, J.; Wu, X.; Zheng, B.; Chen, J.; Sui, X.; Zhang, S.; Shi, J.; Du, W.; Zhong, Y.; Wang, Q.; Zhang, Q.; Pan, A.; Liu, X. Enhanced Trion Emission and Carrier Dynamics in Monolayer WS2 Coupled with Plasmonic Nanocavity. *Adv. Opt. Mater.* **2020**, *8*, No. 2001147.
(40) Liu, R.; Wang, F.; Liu, L.; He, X.; Chen, J.; Li, Y.; Zhai, T. Band Alignment Engineering in Two-Dimensional Transition Metal Dichalcogenide-Based Heterostructures for Photodetectors. *Small Struct.* **2021**, *2*, No. 2000136.
(41) Zhang, S.; Tang, F.; Liu, J.; Che, W.; Su, H.; Liu, W.; Huang, Y.; Jiang, Y.; Yao, T.; Liu, Q.; Wei, S. MoS2-Coated ZnO Nanocomposite as an Active Heterostructure Photocatalyst for Hydrogen Evolution. *Radiat. Phys. Chem.* **2017**, *137*, 104−107.
(42) Liu, S.; Li, B.; Kan, H.; Li, M.-Y.; Xie, B.; Jiang, S.; Zhu, X. Enhanced Sensitivity and Response Speed of Graphene Oxide/ZnO Nanorods Photodetector Fabricated by Introducing Graphene Oxide in Seed Layer. *J. Mater. Sci. Mater. Electron.* **2017**, *28*, 15891−15898.
(43) Palm, K. J.; Murray, J. B.; Narayan, T. C.; Munday, J. N. Dynamic Optical Properties of Metal Hydrides. *ACS Photonics* **2018**, *5*, 4677−4686.
(44) Ghosh, P.; Gorachand, E. D. *Handbook of Optical Constants of Solids*; Academic Press: San Diego, 1998.
(45) Zhang, Z.; Ning, Y.; Fang, X. From Nanofibers to Ordered ZnO/NiO Heterojunction Arrays for Self-Powered and Transparent UV Photodetectors. *J. Mater. Chem. C* **2019**, *7*, 223−229.
(46) Rana, V. S.; Rajput, J. K.; Pathak, T. K.; Purohit, L. P. Multilayer MgZnO/ZnO Thin Films for UV Photodetectors. *J. Alloys Compd.* **2018**, *764*, 724−729.
(47) Tang, R.; Han, S.; Teng, F.; Hu, K.; Zhang, Z.; Hu, M.; Fang, X. Size-Controlled Graphene Nanodot Arrays/ZnO Hybrids for High-Performance UV Photodetectors. *Adv. Sci.* **2018**, *5*, No. 1700334.
(48) Mishra, M.; Gundimeda, A.; Garg, T.; Dash, A.; Das, S.; Vandana; Gupta, G. ZnO/GaN Heterojunction Based Self-Powered Photodetectors: Influence of Interfacial States on UV Sensing. *Appl. Surf. Sci.* **2019**, *478*, 1081−1089.
(49) Cossuet, T.; Resende, J.; Rapenne, L.; Chaix-Pluchery, O.; Jiménez, C.; Renou, G.; Pearson, A. J.; Hoye, R. L. Z.; Blanc-Pelissier, D.; Nguyen, N. D.; Appert, E.; Muñoz-Rojas, D.; Consonni, V.; Deschanvres, J. L. ZnO/CuCrO2 Core−Shell Nanowire Heterostructures for Self-Powered UV Photodetectors with Fast Response. *Adv. Funct. Mater.* **2018**, *28*, No. 1803142.
(50) Liu, S.; Li, M. Y.; Zhang, J.; Su, D.; Huang, Z.; Kunwar, S.; Lee, J. Self-Assembled Al Nanostructure/ZnO Quantum Dot Heterostructures for High Responsivity and Fast UV Photodetector. *Nano-Micro Lett.* **2020**, *12*, No. 114.
(51) Hoang Tran, M.; Park, T.; Hur, J. Solution-Processed ZnO:Graphene Quantum Dot/Poly-TPD Heterojunction for High-Performance UV Photodetectors. *Appl. Surf. Sci.* **2021**, *539*, No. 148222.
(52) Hosseini, Z. S.; Bafrani, H. A.; Naseri, A.; Moshfegh, A. Z. High-Performance UV-Vis-NIR Photodetectors Based on Plasmonic Effect in Au Nanoparticles/ZnO Nanofibers. *Appl. Surf. Sci.* **2019**, *483*, 1110−1117.
(53) Peng, M.; Wang, Y.; Shen, Q.; Xie, X.; Zheng, H.; Ma, W.; Wen, Z.; Sun, X. High-Performance Flexible and Broadband Photodetectors Based on PbS Quantum Dots/ZnO Nanoparticles Heterostructure. *Sci. China Mater.* **2019**, *62*, 225−235.
(54) Zhu, Y.; Song, Z.; Zhou, H.; Wu, D.; Lu, R.; Wang, R.; Wang, H. Self-Powered, Broadband Perovskite Photodetector Based on ZnO Microspheres as Scaffold Layer. *Appl. Surf. Sci.* **2018**, *448*, 23−29.
(55) Benyahia, K.; Djeffal, F.; Ferhati, H.; Bendjerad, A.; Benhaya, A.; Saidi, A. Self-Powered Photodetector with Improved and Broadband Multispectral Photoresponsivity Based on ZnO-ZnS Composite. *J. Alloys Compd.* **2021**, *859*, No. 158242.

https://doi.org/10.1021/acsanm.1c03748
ACS Appl. Nano Mater. XXXX, XXX, XXX−XXX